Inverse Design of a Hybrid Mie-Tamm Photonic Structure as a Highly Directional Gigahertz Single-Photon Source

J.M. Llorens[*] and B. Alén

Instituto de Micro y Nanotecnología (IMN)−Centro Nacional de Microelectrónica (CNM), Consejo Superior de Investigaciones Científicas (CSIC) [Campus of International Excellence (CEI) La Universidad Autónoma de Madrid (UAM) + CSIC] Isaac Newton, 8, Tres Cantos, Madrid E-28760, Kingdom of Spain

We present a photonic structure in which Mie, Tamm, and surface-plasmon optical modes can be tailored to enhance the brightness of an embedded single-photon emitter. Contrary to most proposals, the structure is designed for excitation and collection through the substrate side. The front surface can be used instead to arrange metal contacts which serve the purpose of both electrical gates and optical mirrors. The design is particularized for InGaAs quantum dots on GaAs, resulting in an out-coupled single-photon rate exceeding 3 GHz in a cone of narrow numerical aperture (NA = 0.17). The fabrication tolerances are also discussed.

I. INTRODUCTION

A single-photon source (SPS) with an emission rate beyond 1 GHz is a key element in the field of quantum communications and linear quantum computation [1,2]. An ideal SPS requires a near-unity brightness, purity, and indistinguishability [3]. This is particularly relevant for scalable quantum information processing [4]. A major obstacle in obtaining efficient sources is not related to the quantum efficiency of the emission process but to the difficulty in extraction of the emitted photons from a planar surface. The high refractive index of semiconductors defines a narrow solid angle, free of total internal reflection. Taking as an example the GaAs-air interface, roughly 98% of the emitted photons are trapped within the sample. By placing a planar mirror in close proximity to the emitter, this limit can be raised, increasing the extraction from $1/4n^2$ to $1/n^2$, i.e., by a factor of 4 [5]. To further circumvent this limitation, three-dimensional photonic structures are necessary, which either act on the near field of the emission, as do textured surfaces or micropillars, or in its far field, as do solid immersion lenses [6]. The extraction problem can be defined as a molding of the wave front to funnel the light into a solid angle that is as narrow as possible. If a large extraction is combined with a large

Purcell factor (F_P) [7], the performance of the source can be increased even further under continuous-wave excitation or under pulsed excitation when the excitation repetition rate matches the inverse of the decay rate. This applies particularly in quantum key distribution (QKD), where the secret key rate is proportional to the product of the emission rate and collection efficiency, i.e., the total collected photon number N_{ph} [8]. Micropillars and microlenses are very successful technologies to increase the brightness of single-photon sources [9,10]. The combination of a high-finesse planar distributed Bragg reflector together with a high aspect ratio of tapered micropillars allows for a very smooth extraction of the light from the semiconductor. Microlenses also offer excellent collection efficiencies [11,12] but limited F_P, mainly due to the large volume compared with the emission wavelength in the semiconductor. A better trade-off between the collection efficiency and F_P is found in the circular Bragg gating (CBG), also known as a bull's eye. The best performance reported so far is for upper extraction with a CBG written in a slab surrounded by air resting on a SiO_2/Ag support [13–15].

In this work, we analyze single-photon emitters embedded in a cylinder defined vertically by a bottom distributed Bragg reflector (DBR) and a top metallic mirror [16] and laterally by dielectric confinement with a low-refractive-index layer. The aim is to optimize F_P and the collection efficiency of single photons at the substrate-air interface. In this way, the top metallic mirror can be used as an electrical contact to switch the single-photon emitter on and off or tune its properties. Combined with an embedded excitation source underneath, this design could be used to build a monolithic electrically driven and tunable SPS [17].

---

[*]jose.llorens@csic.es

Planar asymmetric cavities harness optical Tamm states (OTSs) and can exhibit very high Q values [18–21]. However, their planar geometry does not provide lateral confinement, a limitation that has been partially alleviated in the past by reducing the radial extension of the metallic layer [22–24]. Increased performance can be obtained by substituting the homogeneous-cavity medium with a low-refractive-index dielectric layer embedding a high-refractive-index cylinder, as explained below. As a result, Mie-type resonances appear that enhance the electric field [25]. Furthermore, the overlap of such Mie resonances in the cylinder with the OTSs of the embedded dielectric layer increases F_P and steers the emitted light into highly directional cones of light. Surface-plasmon resonances near the metallic layer also play a role and are taken into account to avoid nonradiative losses. The sketch presented in Fig. 1 graphically depicts the four main parts of the optical Mie-Tamm cavity (OMTC) just described. From top to bottom, we find the metallic layer, the dielectric layer, the cylinder in which the quantum emitter is embedded [26], and the $\lambda/4$ DBR. With these elements, the emission is steered toward the substrate, where an antireflective coating (ARC) prevents back reflections. At this point, an optical fiber could be applied directly or by using secondary optics. Its design is omitted from the current study.

This design can be adapted to different quantum emitters, such as nitrogen-vacancy centers in diamond [27], molecules [28], or two-dimensional materials [29,30] and wavelength combinations. Without loss of generality, we analyze the optimization of OMTC structures on GaAs-embedded single self-assembled InGaAs quantum dots (QDs), a SiO_2 dielectric layer, and an AlAs/GaAs DBR. These QDs show excellent purity [31] and indistinguishability [32]. Moreover, as these quantum emitters are based

on III-V semiconductors, they can be integrated into photonic integrated circuits [33–35] and even silicon substrates [36]. With these material choices, we present, in what follows, the optimum design parameters to extract from the sample 3.6-GHz single-photon rates in a cone of narrow numerical aperture (NA = 0.17).

The paper is organized as follows. In Sec. II, we describe the methods used to find the optimum parameters for our design. Section III presents the optimization results, the main properties of the OMTC structure, and some design rules derived from the trade-off between fabrication complexity and device performance. In Sec. IV, we discuss in more detail the nature of the modes harnessed by the structure.

II. METHODS

The optical cavity is sketched in Fig. 1(a). The parameters are defined as follows. The top Au mirror thickness is set to 100 nm to reduce losses in the upper space and to reach the saturation region of the phase change [37]. The dielectric layer thickness is defined as $D = h + d$, where h is the cylinder height and d is an auxiliary parameter. The gap between the GaAs cylinder and the Au mirror is assumed to be occupied by an Au cylinder. Hence, GaAs and Au cylinders take the same radius (r) value. The QD is modeled as a dipole emitter perpendicularly oriented to the cylinder axis. It is located in its axis at a distance z_{QD}. OTSs tend to maximize the field at the mirror interfaces, where the maximum enhancement of the emission might also take place. However, a QD placed close to these interfaces might either be difficult to grow by self-assembly (DBR side) or might suffer from spectral-diffusion broadening and/or luminescence bleach (Au-GaAs side) [38,39].
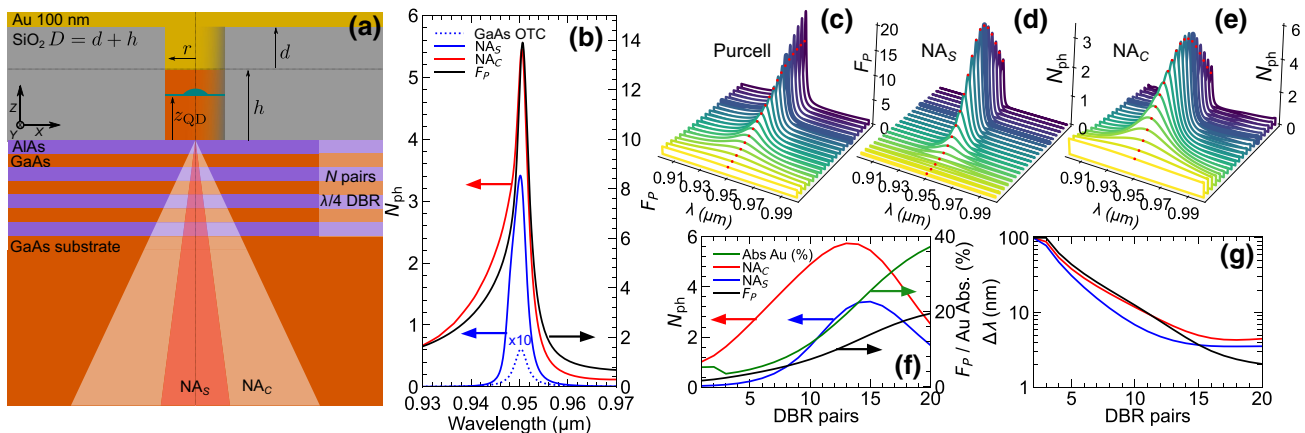

FIG. 1.   (a) A sketch of the OMTC. For a planar GaAs OTC microcavity, the total photon number within GaAs for NA_S magnified by a factor 10 (dotted line). For the optimal structure, the total photon number within GaAs for NA = 0.17 (NA_S) (red line) and NA = 1 (NA_C) (blue line), and FP (black line). The total photon number within GaAs for NA_S of a planar GaAs OTC microcavity magnified by a factor 10 (dotted line). (c)–(e) A fan plot of the evolution of F_P and N_{ph} with N_{DBR} (brightest yellow, $N_{DBR} = 1$; darkest purple, $N_{DBR} = 20$; bold line, $N_{DBR} = 15$). The dot in each line points to the target wavelength (950 nm). (f),(g) The dependence of (f) the maximum of the peak and (g) the line width of the emission for NA_C, NA_S, F_P, and absorption in Au.

Two constraints are imposed, $z_{QD} > 10$ nm, the minimum distance to the top DBR surface, and $z_{QD} < h - 50$ nm, the minimum distance to the metallic cylinder. Both constraints are applied to maximize the fabrication feasibility of the device.

We exploit the axial symmetry of the system to speed up the solution of Maxwell's equations, where the dipole emission asymmetry is handled by an expansion in Fourier modes [26]. Perfectly matching layers are added to the boundary of the simulation region. The numerical solution is performed by the finite-element method, using the commercially available software-package JCMsuite (ver. 4.5; JCMwave GmbH, Germany). The refractive indexes of intrinsic GaAs and AlAs at low temperature are computed using the dispersion model in Ref. [40], with that of SiO_2 from Ref. [41], that of Si_3N_4 from Ref. [42], and that of Au from Ref. [43].

The many resonances that occur in this kind of system naturally call for global optimization methods [44–46]. In our case, the optimization is performed in two stages using the monotonic basin-hopping method, with a 10% variation of the free parameters: r, h, D, and z_{QD}. In the first stage, the structure is locally optimized from a starting point and taken as a seed. In the second step, the parameters are varied randomly within a prescribed range. Subsequent iterations finish when no improvement is found after a limited number of trials (five in our case). As a local optimizer, we use the BOBYQA algorithm [47] implemented in the NLopt library [48]. The whole optimization is performed with the PAGMO library [49]. The objective function is defined to maximize the emission within a very narrow cone at the target wavelength of $\lambda_0 = 950$ nm. Without loss of generality, we set the cone aperture NA = 0.17 (NA_S), as a representative value of a highly directional emission, i.e., roughly a sixth of the critical angle NA = 1 (NA_C). As a figure of merit (FOM), we use the total photon number (N_{ph}), defined as the collection efficiency (CE) within a NA_S times F_P. The N_{ph} has a straightforward interpretation. If one assumes a typical exciton emission radiative lifetime of 1 ns in bulk GaAs ($F_P = 1$), the optimized total photon number can be related to an extracted single-photon rate in the gigahertz range. The CE is computed from the far-field projection of the electric field within a homogeneous GaAs medium representing the substrate ($\mathbf{E}(\theta, \phi)$, θ and ϕ being the polar and azimuthal angles in spherical coordinates). The outcoupling to air, i.e., beyond the substrate interface, is also considered by introducing a $\lambda/4$ Si_3N_4 ARC [50]. The final CE and N_{ph} values on air result from the propagation of $\mathbf{E}(\theta, \phi)$ within homogeneous intrinsic GaAs and its transmission through the GaAs-Si_3N_4-air interfaces calculated by the transfer matrix method for s- and p-polarized light. Absorption losses are considered through the tabulated complex refractive index of each material but at the design wavelength do not lead to additional propagation losses.

III. RESULTS

By inspection of Fig. 1(a), we can envisage the two extreme cases of our design. For zero cylinder diameter, the structure is a SiO_2 optical Tamm cavity (OTC) and for very large diameters it operates as a GaAs OTC. For cylinder sizes similar to the wavelength, Mie resonances are expected and we can think of an OMTC cavity. Resonances in an OTC follow the same pattern as in the Fabry-Perot (FP) cavity [19], i.e., $d_N = d_0 + N\lambda/2n$, where d_0 is the minimum resonant thickness, n is the refractive index, and $N = 0, 1, \ldots$ is the FP order. As a seed value in the optimization, we consider the thickness of the FP $N = 1$ in a SiO_2 OTC at 950 nm, i.e., $D = 460$ nm. Analogously, we set the initial height of the cylinder to the thickness of the same resonance in a GaAs OTC, i.e., $h = 183$ nm. The other parameters are set to arbitrary initial values, $r = 200$ nm and $z_{QD} = h/2$, and we let the algorithm find the optimal values. The optimal structure is found for $r = 223$ nm, $h = 361$ nm, and $D = 459$ nm, the dipole being located at 304 nm from the cylinder base. The optimal number of DBR pairs (N_{DBR}) is found to be 15, as explained below. Figure 1(b) shows the resonances found around 950 nm for F_P and N_{ph} for light collected within NA_C and NA_S within GaAs. At resonance, the maximum F_P is 12.4 and the maximum N_{ph} is 5.3 (3.6) for NA_C (NA_S), respectively. The line shape of the spectrum also depends on the NA. At narrow collection angles, it exhibits a Lorentzian line shape of 3.7-nm full width at half maximum (FWHM), while at the full extraction angle the line shape becomes asymmetric, with FWHM=5 nm.

It is worth comparing the value $N_{ph} = 3.6$ found for NA_S with that of two reference structures. In a substrate with a mirror, the collection efficiency is approximately $1/n^2$ [5]. For $\lambda_0 = 950$ nm, $n_{GaAs} = 3.46$, and assuming $F_P \approx 1$, we obtain $N_{ph} = 0.083$ for NA_C and $N_{ph} = 0.0024$ for NA_S. The second structure is a GaAs OTC of $h = 179$ nm, i.e., the asymmetric cavity described by Benisty et al. in Ref. [16]. By placing the dipole at 10 nm from the DBR (the lower bound considered in our calculations), a $F_P = 1.4$ results in the spectrum shown in Fig. 1(b) as a dashed line with a maximum $N_{ph} = 0.061$. Our design, introducing the Mie-Tamm hybrid structure, with the QD located at least 50 nm away from the nearest surface, improves the bare case by a factor of 1500 and the GaAs-OTC case by a factor of 60—a clear signature of the advantages brought about by the OMTC scheme.

A key element of the design is the DBR, as it is responsible for the OTS. Figures 1(c)–1(e) show the evolution with an increasing number of DBR pairs of F_P and N_{ph} resonances found around 950 nm. The F_P peak intensity increases monotonically in the studied range, reaching a maximum value of 20 for 20 DBR pairs [Fig. 1(f)]. Meanwhile, the N_{ph} resonances have two different regimes where the peak intensity first increases up to 14–15 pairs

depending on the NA and then decreases with the number of DBR pairs. This is the expected dependence for collection through the substrate side, since the transparency of the DBR mirror decreases with N_{DBR}. In such a case, there is a trade-off between the emission and collection enhancement throughout the substrate and the light storage in the cavity, which is also modulated by absorption at the Au gold mirror and other losses. Indeed, at the N_{ph} maximum, the total scattered power is 75% (72% in the downward direction) and the Au absorption is 25% (NA = NA$_S$). Beyond that point, the absorption increases to 37%, as shown in Fig. 1(f).

The resonance line-width evolution is shown in Fig. 1(g). Again, the F_P line width shows a monotonic dependence, continuously narrowing in the studied range, while the N_{ph} line width first narrows downs and then saturates beyond approximately 15 DBR pairs. This line-width dependence determines how challenging the spectral matching between the QD emission peak and the cavity resonance will be [51]. Depending on the fabrication uncertainty, it could be beneficial to reduce N_{DBR} from 15 to 9 to increase the line width from 3.7 nm to 8.7 nm. The penalty is a reduction of N_{ph} from 3.6 to 1.2 GHz for NA$_S$. This trade-off between performance and fabrication yield can be anticipated from our analysis.

High directionality is demanded to overcome total internal reflection at the substrate interface and bring the emitted light out of the sample. Figures 2(a) and 2(b) shows N_{ph} and the CE on air as a function of the NA for varying N_{DBR}. The figure follows the same color scheme as in Figs. 1(c)–1(e). A bolder line is used for $N_{DBR} = 15$. The steep rise of N_{ph} and the CE for small values of the NA is a clear signature of the high directionality of the emission of our design: most of the light has been emitted for NA < 0.5. As shown in the inset by a polar contour plot, the far field is concentrated in a very small NA area and lacks azimuthal dependence. The peak values obtained in air are only 1% smaller than the values reported in Fig. 1, because the transmission is close to one for those angles at which the far field is strong. Beyond NA = 1, the light cannot escape out of the substrate and N_{ph} remains constant. The dashed line represents N_{ph} without the Si$_3$N$_4$ ARC for $N_{DBR} = 15$, showing the importance of this additional layer. Without the ARC, the reduction is 30%.

In Fig. 2(c). the CE values at NA$_C$ and NA$_S$ as a function of N_{DBR} are presented. For NA$_C$ (NA$_S$), the maximum CE is 0.72 (0.29), obtained at an N_{DBR} of 7 (13). A new trade-off is established, depending on which magnitude is maximized. Collection at a large NA requires a small N_{DBR}, while for a narrow NA, a large value of N_{DBR} maximizes both the CE and N_{ph}. The spectral dependence is shown in Fig. 2(d) for an N_{DBR} of 7 (13) at NA$_C$ (NA$_S$), i.e., at the maxima of Fig. 2(c). While the CE at NA$_S$ critically depends on the tuning between resonances, a CE greater than 0.6 can be obtained at NA$_C$ over a much broader band.

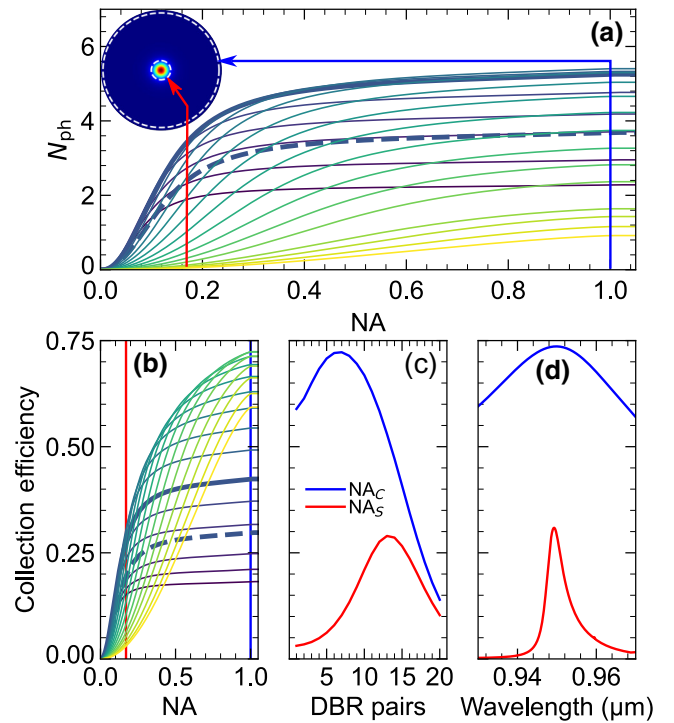

FIG. 2.   (a) The cumulative N_{ph} in air considering an ARC as a function of the NA for different values of N_{DBR} (brightest yellow, $N_{DBR} = 1$; darkest purple, $N_{DBR} = 20$). The inset shows the far-field projection up to NA$_C$. The dashed-line circles mark the NA$_S$ and NA$_C$ values, also indicated by red and blue arrows, respectively. (b) The equivalent plot for the CE. (c) The evolution of the CE for NA$_S$ and NA$_C$ as a function of N_{DBR}. (d) The CE spectral dependence at $N_{DBR} = 7$ for NA$_C$ and $N_{DBR} = 13$ for NA$_S$. The solid (dashed) bold lines in (a) and (b) correspond to the optimal $N_{DBR} = 15$ with (without) an ARC.

In summary, the target application and the collection setup will ultimately determine the optimal N_{DBR}.

To understand how the optical mode structure varies with the geometrical parameters, we depict in Fig. 3 the dependence of N_{ph} on d, h, or r, while keeping the other two parameters and z_{QD} fixed. The studied range is limited to 500 nm. The SiO$_2$ slab thickness d shows two main resonances, at 423 nm and 98 nm [Fig. 3(a)]. The free spectral range (FSR) is 325 nm, matching $\lambda_0/2n$ in SiO$_2$ very well [19,52]. The GaAs cylinder height h also exhibits two N_{ph} resonances in Fig. 3(a), with FSR = 151 nm. This value differs by 14 nm from $\lambda_0/2n$ in GaAs, as expected, given the limited in-plane extension of the nanocylinder. Meanwhile, r also shows two resonances, with FSR = 142 nm. The three-dimensional nature of the nanocavity makes their study more involved. Indeed, we study the interplay between h and r in more detail in Sec. IV.

This parameter exploration is done at fixed λ_0. To get a more comprehensive picture, spectral dependence can be added to the analysis. Figures 3(b) and 3(c) show contour plots of N_{ph} in logarithmic scale for different values
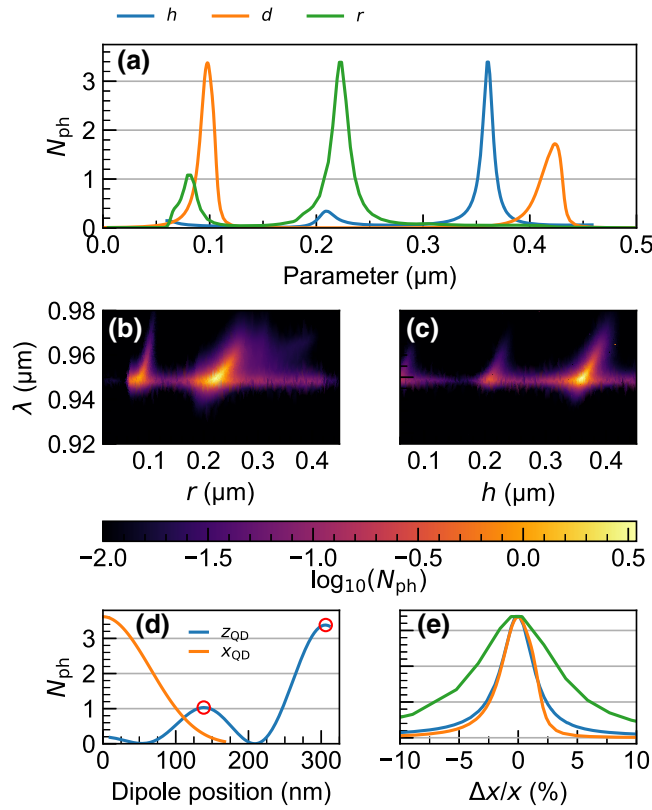
FIG. 3.   (a) The dependence of N_{ph} on the cylinder height h, the radius r, and the dielectric thickness relative to height d, as calculated for NA_S within GaAs. N_{ph} finds its maximum at $r = 223$ nm, $h = 361$ nm, and $d = 98$ nm. (b),(c) Logarithmic plots of N_{ph} at NA_S as a function of (b) λ and r and (c) λ and h. (d) The position of the dipole in the cylinder (x_{QD} and z_{QD}) The two maxima in z_{QD} discussed in the text are indicated by open circles. (e) The relative deviation with respect to the optimal value.

of r and h and emission wavelengths. The emission is negligible except at the design wavelength, λ_0, where the enhancement takes place at particular r and h values, giving rise to the resonances discussed above. Due to an exponential decay of N_{ph} as soon as the cylinder size and wavelength depart from the optimal values, changing the cylinder radius alone does not provide an effective way to spectrally tune the OMTC and the QD in a broad range. Broad spectral tuning can still be done after growth, within the stop band of the DBR (approximately 100 nm), reducing h through etching as necessary in order to target smaller r and λ. Alternatively, N_{DBR} can be reduced as explained above to relax the spectral matching condition.

The last parameters to be discussed are z_{QD} and x_{QD}, the QD off-axis deviation. As shown in Fig. 3(d) for the optimal geometry, N_{ph} exhibits two maxima at z_{QD} 138 and 306 nm. They are rather broad, with FWHMs along the cylinder axis of 76 and 47 nm, respectively. They stem from the overlap with the field distributions shown in Fig. 4(a) which, as discussed in Sec. IV, correspond to the cylinder
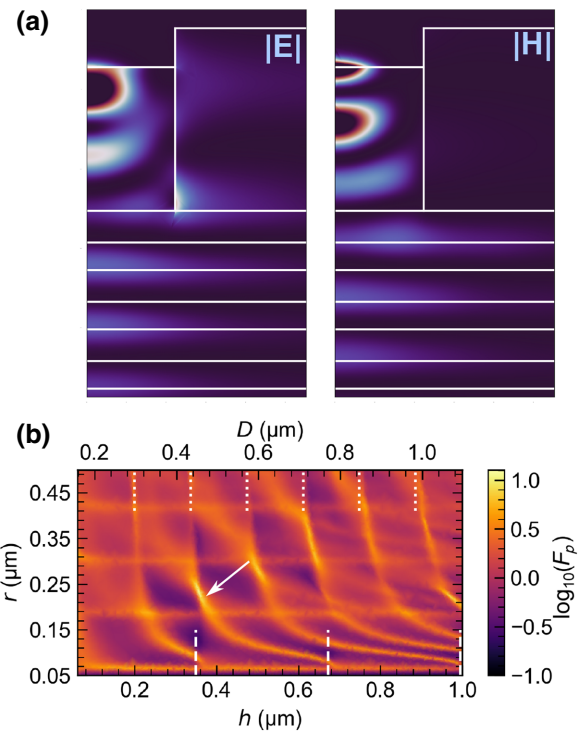

FIG. 4.   (a) The XZ cross section of $|E|$ and $|H|$ of the optimal structure. The structure layout is defined by the white lines. (b) The dependence of F_P in logarithmic scale at 950 nm as a function of r and h for a fixed d. The vertical lines denote the operating wavelength in GaAs (dotted lines) and in SiO$_2$ (dashed lines).

Mie resonance of the OMTC structure. These field distributions tend to occupy a large portion of the nanocavity volume, which is highly beneficial for the spatial matching of the single-photon emitter and the cavity mode. As can be seen in Fig. 3(d), N_{ph} peaks at $x_{QD} = 0$ with an FWHM of 149 nm, well above the typical precision of approximately 40 nm of deterministic nucleation site-control methods [53–55].

The results just presented can be used to discuss the fabrication feasibility of the proposed design. Figure 3(e) shows the N_{ph} evolution upon a change of the three most critical parameters around its optimum value. h and d are the most demanding, with 3.3% and 4.4% tolerance each. This stems from resonance FWHMs of 12 nm and 16 nm, respectively. The less demanding parameter is r, which exhibits a FWHM (tolerance) of 18 nm (8.2%). Reported experimental values of statistical variations of electron-beam lithographic micropillars (30 nm in 2.0-μm diameter) and nanocylinders in metasurfaces (5 nm in 114-nm diameter) can be as low as 1.5% [56] and 4% [57], respectively. These values are below the required tolerance of r in our case. Controlling the SiO$_2$ thickness within tolerance can be done by optically monitored dry etching to reach the target value from an overgrown sample.

The results in Fig. 3(e) indicate that even with deviations that are twice as large, N_{ph} can reach 0.8 within NA_S (or 800-MHz single-photon count rates extracted from the sample).

Depending on the aspect ratio of the structure, the surface roughness has a great impact on the optical properties. In the case of nanopillars with large aspect ratios, diffraction at the wall roughness produces scattering of the guided mode into other modes, resulting in a reduction of the Q factor [9]. As the height of the micropillar decreases and the diameter increases toward a shallow cylinder, the FSR between adjacent Mie resonances becomes larger and hence a weaker scattering by the surface roughness is expected. Similarly, the exciton line width can be affected by surface states and traps at a rough surface. Liu *et al.* [58] have performed a study of these issues on QD-based photonic nanostructures, including surface passivation with Al_2O_3. They have shown that the quantum efficiency is not affected at all in the proximity of dry-etched surfaces 50–300 nm away from the QD. At 150 nm, the peak broadens by a factor of 1.38 and, at 300 nm, the surface no longer affects the line width. In the whole range, the $g^{(2)}(0)$ value remains constant. In our case, we find the optimal $r = 223$ nm and thus a broadening factor of the order of 1.2 in the exciton emission line could be expected. As a final remark, the 55 nm separation between the QD and the metallic mirror might compromise the indistinguishability of the single photons, though being larger than typical distances employed in plasmon antennas for quantum applications [59,60]. This issue can be solved in the current design by moving the QD to the secondary maximum at 138 nm (223 nm below the interface) [see Fig. 3(d)], trading indistinguishability for brightness. The expected change in the CE is from 29% to 24.2% In future designs, the physical and geometrical parameters of the structure could be modified to increase that separation. From this discussion, we conclude that OMTC designs such as the one presented here are feasible from the fabrication point of view.

IV. DISCUSSION

The interplay between the OTS and the Mie resonances can be inferred from the field distribution shown for the optimized structure in Fig. 4(a). The white lines indicate the different regions depicted in Fig. 1(a). In the SiO_2 slab (top right) a node line spans parallel to the substrate. This corresponds to the OTS resonance used as a seed in the optimization, i.e., a full oscillation of $\lambda_0/2$ in SiO_2 fits within the structure. In the DBR region (bottom-half region), an oscillation of the electric field in phase with the DBR period is found. Indeed, despite the three-dimensional character of the cylinder, the wave front is parallel to the interfaces of the DBR, leading to the narrow directionality of the emission. The field distribution inside the cylinder clearly shows the excitation of a Mie

resonance as anticipated in the discussion of x_{QD}. In this particular case, $|E|$ shows two ring structures and $|H|$ shows two antinodes. This field distribution is characteristic of a magnetic multipole resonance [61–63] and has previously been reported for a horizontal dipole located near the top or bottom surfaces in free-standing cylinders [64].

The properties of the OMTC cavity are better understood from the evolution of F_P as a function of r and h for fixed d, i.e., D changes with h. Figure 4(b) shows the corresponding contour plot with all the resonances excited in the system. The white arrow points to the optimal one. We recall that r determines whether the structure behaves as a SiO_2 OTC ($r \ll$) or as a GaAs OTC ($r \gg$). For $r = 50$ nm, discrete resonances appear, with an FSR of $\lambda_0/2$ corresponding to the SiO_2 OTC, and are indicated by vertical white dashed lines. At $r = 450$ nm, another family of resonances appears, with an FSR of $\lambda_0/2$, which is associated with the GaAs OTC by a series of vertical white dotted lines. The modal structure of the cylinder offers enough flexibility to smoothly connect both limits. The optimal structure appears when h gets close to the GaAs-OTC FP $N = 2$. Around this value of h, the SiO_2-OTC FP $N = 1$ mode is also excited. This explains why $|E|$ exhibits two nodes in the cylinder while exhibiting only one in the SiO_2 slab in Fig. 4(a). The Purcell-factor contour plot also reveals a series of horizontal resonances crossing the Mie resonances at regular r intervals. They are related to the excitation of surface plasmon polaritons at the GaAs-Au interface, as explained below.

Figure 5(a) shows a line plot of F_P as a function of r, fixing h at the optimal value. The blue line stems from the absorption in the Au mirror, calculated as a fraction of the total emitted power as explained above. We distinguish two series of mode peaks labeled O_{1n} and M_n, respectively. Their different nature is revealed by plotting in Figs. 5(b)–5(g) the cross sections of $Re(E_y)$ in the X-Y plane (top) and the X-Z plane (bottom) for each mode. The field distributions in Figs. 5(b), 5(d), 5(f), and 5(g) are clearly confined in the GaAs-Au interface, while those in Figs. 5(c) and 5(e) occupy the volume of the GaAs cylinder. In view of these results, the latter are attributed to Mie resonances of different magnetic multipole order (M_1 and M_2), while the former can be related to surface plasmon polaritons (SPPs).

Our analysis reveals that in the region of the GaAs-Au interface, the metallic contact acts as a circular plasmonic patch nanoantenna [65]. In our configuration, the dipole is oriented parallel to the interface and excites the family of odd modes labeled as O_{mn} [66]; in particular, the modes with $m = 1$, the first azimuthal mode number, and different n radial ones. The FSR between the O_{1n} peaks [the dotted vertical lines in Fig. 5(a)] compares very well with the half wavelength of the SPP $\lambda_{SPP} = \lambda_0\sqrt{(Re(\varepsilon_{Au}) + \varepsilon_{GaAs})/Re(\varepsilon_{Au})\varepsilon_{GaAs}}$ [67], being equal to
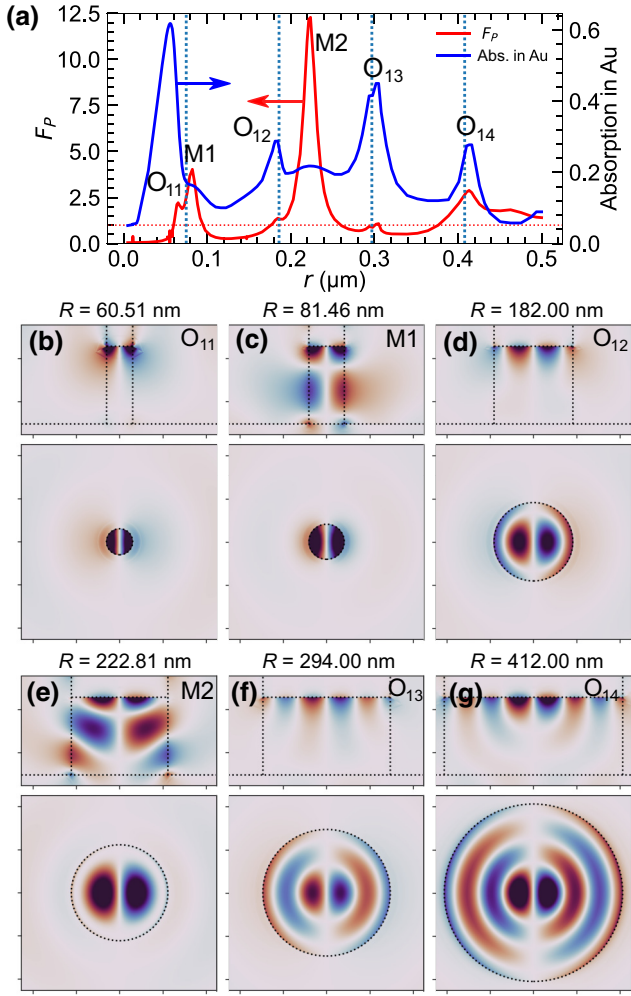
FIG. 5. (a) The evolution of F_P and absorption in Au as a function of r for the optimal h. The horizontal red dotted line indicates unity F_P. The vertical blue dotted lines are spaced by $\lambda_{\text{SPP}}/2$ (see the main text). (b)–(g) Top: the contour plot of $\text{Re}(E_y)$ for each mode in an XZ cross section centered at the origin (the dotted lines are the profile of the structure) Bottom: the analogous XY cross section for each mode close to the GaAs-Au interface. All plots use the same color scale between negative (red) and positive (blue) field values.

109 nm. It also agrees very well with the resonance condition of circular-patch nanoantennas [65]:

$$2\text{Re}(k_{\text{SPP}})r_n + \phi^r = 2x_n, \qquad (1)$$

where r_n is the nth radius at resonance, ϕ^r is the phase origin, k_{SPP} is the SPP wave vector, and x_n is the nth zero of the J_1 Bessel function. The phase ϕ^r depends on r but, as a first approximation, we can assume that the dependence is very weak. Hence, $r_{n+1} - r_n = (x_{n+1} - x_n)/\pi\,\lambda_{\text{SPP}}/2$. In addition, this verifies that $(x_{n+1} - x_n) \approx \pi$ for small n and therefore the FSR is very close to $\lambda_{\text{SPP}}/2$, as expected. This

is the final confirmation of the nature and position of the different SPP resonances found in our system.

One needs to be aware of the presence of these SPP resonances when designing an OMTC structure. They can introduce large parasitic losses, jeopardizing the enhancement of F_P and N_{ph} produced by the combination of Mie and OTS resonances. So, even if our design is fully scalable to other wavelengths, e.g., 1.3 μm or 1.5 μm, just by rescaling the DBR, r, h, and D accordingly, some care needs to be taken in case the material dispersion introduces the unwanted overlap between SPPs and Mie resonances just described. Otherwise, a penalty would be paid in performance.

We finish this section by reviewing the main advantages of our approach. The backward collection through the substrate side allows us to use a metallic optical mirror and Ohmic contact to drive and tune electrically the emission. The cylinder height of 350 nm allows us to fit a p-i-n diode without any problems. If driving is not necessary and fine control of the charge and wavelength is desired instead, an ultrathin 162.5-nm p-i-n-i-n diode [68] or a simpler Schottky diode [69] could be used. In all cases, the QD-to-surface distances can be adapted and values of 100–250 nm are typical. The doping layers will introduce some additional losses, without a significant impact on the expected device performance. Representative values of the absorption in GaAs at $\lambda \approx 1$ μm are $\alpha = 11(5)$ cm^{-1} per 10^{18} cm^{-3} p-type (n-type) doping [70] and hence the refractive-index imaginary part of the doped regions would result in 8×10^{-5} (4×10^{-5}). The design relies on a semitransparent DBR located underneath the QD, which enables optical excitation through a built-in [17,71–73] or external laser diode. Secondary micro-optical elements could be located at the substrate to excite and/or collect the photoluminescence, which would not interfere spatially with the primary photonic nanocavity in which the QD is embedded. Compared with photonic crystal microcavities, the removal of material surrounding the cylinder reduces the chances of unwanted luminescence from nearby QDs, contributing to the optical mode. Also, the Mie-resonance in-plane extension fills a large proportion of the cavity cross section, increasing the chances of good spatial overlap in low-density QD samples without requiring deterministic methods. From the performance point of view, the directionality of the emission is superb and allows large single-photon extraction rates within a low NA even with moderate values of the Purcell factor. In addition, the design is fully scalable and manufacturable with current microplanar fabrication techniques.

V. CONCLUSIONS

We introduce and analyze a photonic structure to enhance the brightness of single-photon sources with very high efficiency. Via a global optimization method, we find

the optimal structure parameters for the case of InGaAs QDs embedded in GaAs. From the analysis of the resulting structure, we show that the enhancement is based on the cooperation of Tamm and Mie resonances intertwined in our design. We predict a N_{ph} of 3.6 for a narrow extraction cone of NA = 0.17 and one of 5.3 for the critical angle extraction cone (NA = 1), which boosts the single-photon extraction rate to the gigahertz range. These values are significantly larger than those attainable in a bare optical Tamm cavity or a bare Mie structure of comparable size. Therefore, we term our proposal an optical Mie-Tamm cavity (OMTC).

[1] S. Pirandola, U. L. Andersen, L. Banchi, M. Berta, D. Bunandar, R. Colbeck, D. Englund, T. Gehring, C. Lupo, C. Ottaviani, J. L. Pereira, M. Razavi, J. S. Shaari, M. Tomamichel, V. C. Usenko, G. Vallone, P. Villoresi, and P. Wallden, Advances in quantum cryptography, Adv. Opt. Photon. **12,** 1012 (2020).

[2] C.-Y. Lu and J.-W. Pan, Quantum-dot single-photon sources for the quantum Internet, Nat. Nanotechnol. **16,** 1294 (2021).

[3] P. Senellart, G. Solomon, and A. White, High-performance semiconductor quantum-dot single-photon sources, Nat. Nanotechnol. **12,** 1026 (2017).

[4] H. Wang, J. Qin, X. Ding, M.-C. Chen, S. Chen, X. You, Y.-M. He, X. Jiang, L. You, Z. Wang, C. Schneider, J. J. Renema, S. Höfling, C.-Y. Lu, and J.-W. Pan, Boson Sampling with 20 Input Photons and a 60-Mode Interferometer in a 10^{14}-Dimensional Hilbert Space, Phys. Rev. Lett. **123,** 250503 (2019).

[5] H. Benisty, H. De Neve, and C. Weisbuch, Impact of planar microcavity effects on light extraction-Part I: Basic concepts and analytical trends, IEEE J. Quantum Electron. **34,** 1612 (1998).

[6] W. Barnes, G. Björk, J. Gérard, P. Jonsson, J. Wasey, P. Worthing, and V. Zwiller, Solid-state single photon sources: Light collection strategies, Eur. Phys. J. D **18,** 197 (2002).

[7] F. Liu, A. J. Brash, J. O'Hara, L. M. P. P. Martins, C. L. Phillips, R. J. Coles, B. Royall, E. Clarke, C. Bentham, N. Prtljaga, I. E. Itskevich, L. R. Wilson, M. S. Skolnick,

[8] and A. M. Fox, High Purcell factor generation of indistinguishable on-chip single photons, Nat. Nanotechnol. **13,** 835 (2018).

[8] T. Kupko, M. von Helversen, L. Rickert, J.-H. Schulze, A. Strittmatter, M. Gschrey, S. Rodt, S. Reitzenstein, and T. Heindel, Tools for the performance optimization of single-photon quantum key distribution, npj Quantum Inf. **6,** 1 (2020).

[9] S. Reitzenstein and A. Forchel, Quantum dot micropillars, J. Phys. D: Appl. Phys. **43,** 033001 (2010).

[10] X. Ding, Y. He, Z.-C. Duan, N. Gregersen, M.-C. Chen, S. Unsleber, S. Maier, C. Schneider, M. Kamp, S. Höfling, C.-Y. Lu, and J.-W. Pan, On-Demand Single Photons with High Extraction Efficiency and Near-Unity Indistinguishability from a Resonantly Driven Quantum Dot in a Micropillar, Phys. Rev. Lett. **116,** 020401 (2016).

[11] S. Morozov, M. Gaio, S. A. Maier, and R. Sapienza, Metal-Dielectric Parabolic Antenna for Directing Single Photons, Nano Lett. **18,** 3060 (2018).

[12] M. Schmidt, M. V. Helversen, S. Fischbach, A. Kaganskiy, R. Schmidt, A. Schliwa, T. Heindel, S. Rodt, and S. Reitzenstein, Deterministically fabricated spectrally-tunable quantum dot based single-photon source, Opt. Mat. Express **10,** 76 (2020).

[13] H. Wang, H. Hu, T.-H. Chung, J. Qin, X. Yang, J.-P. Li, R.-Z. Liu, H.-S. Zhong, Y.-M. He, X. Ding, Y.-H. Deng, Q. Dai, Y.-H. Huo, S. Höfling, C.-Y. Lu, and J.-W. Pan, On-Demand Semiconductor Source of Entangled Photons Which Simultaneously Has High Fidelity, Efficiency, and Indistinguishability, Phys. Rev. Lett. **122,** 113602 (2019).

[14] L. Rickert, T. Kupko, S. Rodt, S. Reitzenstein, and T. Heindel, Optimized designs for telecom-wavelength quantum light sources based on hybrid circular Bragg gratings, Opt. Express **27,** 36824 (2019).

[15] S. Kolatschek, C. Nawrath, S. Bauer, J. Huang, J. Fischer, R. Sittig, M. Jetter, S. L. Portalupi, and P. Michler, Bright Purcell Enhanced Single-Photon Source in the Telecom O-Band Based on a Quantum Dot in a Circular Bragg Grating, Nano Lett. **21,** 7740 (2021).

[16] H. Benisty, H. De Neve, and C. Weisbuch, Impact of planar microcavity effects on light extraction-Part II: Selected exact simulations and role of photon recycling, IEEE J. Quantum Electron. **34,** 1632 (1998).

[17] B. Alén, D. Fuster, Y. González, and L. González, Device for emitting single photons or entangled photon pairs (EP3361516B1, 2017-02-08).

[18] M. Kaliteevski, I. Iorsh, S. Brand, R. A. Abram, J. M. Chamberlain, A. V. Kavokin, and I. A. Shelykh, Tamm plasmon-polaritons: Possible electromagnetic states at the interface of a metal and a dielectric Bragg mirror, Phys. Rev. B **76,** 165415 (2007).

[19] H. Zhou, G. Yang, K. Wang, H. Long, and P. Lu, Multiple optical Tamm states at a metal-dielectric mirror interface, Opt. Lett. **35,** 4112 (2010).

[20] M. E. Sasin, R. P. Seisyan, M. A. Kalitteevski, S. Brand, R. A. Abram, J. M. Chamberlain, A. Y. Egorov, A. P. Vasil'ev, V. S. Mikhrin, and A. V. Kavokin, Tamm plasmon polaritons: Slow and spatially compact light, Appl. Phys. Lett. **92,** 251112 (2008).

[21] C. Symonds, S. Azzini, G. Lheureux, A. Piednoir, J. M. Benoit, A. Lemaitre, P. Senellart, and J. Bellessa,

High quality factor confined Tamm modes, Sci. Rep. **7,** 1 (2017).

[22] O. Gazzano, S. M. de Vasconcellos, K. Gauthron, C. Symonds, J. Bloch, P. Voisin, J. Bellessa, A. Lemaitre, and P. Senellart, Evidence for Confined Tamm Plasmon Modes under Metallic Microdisks and Application to the Control of Spontaneous Optical Emission, Phys. Rev. Lett. **107,** 247402 (2011).

[23] T. Braun, V. Baumann, O. Iff, S. Höfling, C. Schneider, and M. Kamp, Enhanced single photon emission from positioned InP/GaInP quantum dots coupled to a confined Tamm-plasmon mode, Appl. Phys. Lett. **106,** 041113 (2015).

[24] M. Parker, E. Harbord, L. Chen, E. Clarke, K. Kennedy, J. Rarity, and R. Oulton, Telecommunication wavelength confined Tamm plasmon structures containing InAs/GaAs quantum dot emitters at room temperature, Phys. Rev. B **100,** 165306 (2019).

[25] S. Bidault, M. Mivelle, and N. Bonod, Dielectric nanoantennas to manipulate solid-state light emission, J. Appl. Phys. **126,** 094104 (2019).

[26] P.-I. Schneider, N. Srocka, S. Rodt, L. Zschiedrich, S. Reitzenstein, and S. Burger, Numerical optimization of the extraction efficiency of a quantum-dot based single-photon emitter into a single-mode fiber, Opt. Express **26,** 8479 (2018).

[27] D. Riedel, I. Sollner, B. J. Shields, S. Starosielec, P. Appel, E. Neu, P. Maletinsky, and R. J. Warburton, Deterministic Enhancement of Coherent Photon Generation from a Nitrogen-Vacancy Center in Ultrapure Diamond, Phys. Rev. X **7,** 031040 (2017).

[28] D. Geng, E. Cabello-Olmo, G. Lozano, and H. Míguez, Tamm Plasmons Directionally Enhance Rare-Earth Nanophosphor Emission, ACS Photon. **6,** 634 (2019).

[29] N. Lundt, S. Klembt, E. Cherotchenko, S. Betzold, O. Iff, A. V. Nalitov, M. Klaas, C. P. Dietrich, A. V. Kavokin, S. Höfling, and C. Schneider, Room-temperature Tamm-plasmon exciton-polaritons with a WSe₂ monolayer, Nat. Commun. **7,** 13328 (2016).

[30] W. L. Zhang, X. J. Li, S. S. Wang, C. Y. Zheng, X. F. Li, and Y. J. Rao, Polaritonic manipulation based on the spin-selective optical Stark effect in the WS₂ and Tamm plasmon hybrid structure, Nanoscale **11,** 4571 (2019).

[31] L. Schweickert, K. D. Jöns, K. D. Zeuner, S. F. Covre da Silva, H. Huang, T. Lettner, M. Reindl, J. Zichi, R. Trotta, A. Rastelli, and V. Zwiller, On-demand generation of background-free single photons from a solid-state source, Appl. Phys. Lett. **112,** 093106 (2018).

[32] A. Thoma, P. Schnauber, M. Gschrey, M. Seifried, J. Wolters, J.-H. Schulze, A. Strittmatter, S. Rodt, A. Carmele, A. Knorr, T. Heindel, and S. Reitzenstein, Exploring Dephasing of a Solid-State Quantum Emitter via Time- and Temperature-Dependent Hong-Ou-Mandel Experiments, Phys. Rev. Lett. **116,** 033601 (2016).

[33] S. Hepp, M. Jetter, S. L. Portalupi, and P. Michler, Semiconductor Quantum Dots for Integrated Quantum Photonics, Adv. Quantum Technol. **2,** 1900020 (2019).

[34] L. Dusanowski, D. Köck, E. Shin, S.-H. Kwon, C. Schneider, and S. Höfling, Purcell-Enhanced and Indistinguishable Single-Photon Generation from Quantum Dots Coupled to On-Chip Integrated Ring Resonators, Nano Lett. **20,** 6357 (2020).

[35] S. Rodt and S. Reitzenstein, Integrated nanophotonics for the development of fully functional quantum circuits based on on-demand single-photon emitters, APL Photonics **6,** 010901 (2021).

[36] C. Shang, Y. Wan, J. Selvidge, E. Hughes, R. Herrick, K. Mukherjee, J. Duan, F. Grillot, W. W. Chow, and J. E. Bowers, Perspectives on Advances in Quantum Dot Lasers and Integration with Si Photonic Integrated Circuits, ACS Photon. **8,** 2555 (2021).

[37] M. Adams, B. Cemlyn, I. Henning, M. Parker, E. Harbord, and R. Oulton, Model for confined Tamm plasmon devices, J. Opt. Soc. Am. B **36,** 125 (2019).

[38] C. F. Wang, A. Badolato, I. Wilson-Rae, P. M. Petroff, E. Hu, J. Urayama, and A. Imamoğlu, Optical properties of single InAs quantum dots in close proximity to surfaces, Appl. Phys. Lett. **85,** 3423 (2004).

[39] J. Liu, R. Su, Y. Wei, B. Yao, S. F. C. d. Silva, Y. Yu, J. Iles-Smith, K. Srinivasan, A. Rastelli, J. Li, and X. Wang, A solid-state source of strongly entangled photon pairs with high brightness and indistinguishability, Nat. Nanotechnol. **14,** 586 (2019).

[40] S. Gehrsitz, F. K. Reinhart, C. Gourgon, N. Herres, A. Vonlanthen, and H. Sigg, The refractive index of $Al_xGa_{1-x}As$ below the band gap: Accurate determination and empirical modeling, J. Appl. Phys. **87,** 7825 (2000).

[41] E. D. Palik, ed., *Handbook of Optical Constants of Solids*, Vol. 3 (Academic press, 1998).

[42] K. Luke, Y. Okawachi, M. R. E. Lamont, A. L. Gaeta, and M. Lipson, Broadband mid-infrared frequency comb generation in a Si_3N_4 microresonator, Opt. Lett. **40,** 4823 (2015).

[43] P. B. Johnson and R. W. Christy, Optical constants of the noble metals, Phys. Rev. B **6,** 4370 (1972).

[44] S. Molesky, Z. Lin, A. Y. Piggott, W. Jin, J. Vucković, and A. W. Rodriguez, Inverse design in nanophotonics, Nat. Phot. **12,** 659 (2018).

[45] E. G. Melo, W. Eshbaugh, E. B. Flagg, and M. Davanco, Multiobjective inverse design of solid-state quantum emitter single-photon sources, ACS Photonics (2022), in press, available on-line.

[46] J. Guimbao, L. Sanchis, L. Weituschat, J. Manuel Llorens, M. Song, J. Cardenas, and P. Aitor Postigo, Numerical optimization of a nanophotonic cavity by machine learning for near-unity photon indistinguishability at room temperature, ACS Photon. **9,** 1926 (2022).

[47] M. J. Powell, The BOBYQA algorithm for bound constrained optimization without derivatives. Technical report (2009).

[48] S. G. Johnson, The NLopt nonlinear-optimization package, http://github.com/stevengj/nlopt.

[49] F. Biscani and D. Izzo, A parallel global multiobjective framework for optimization: PAGMO, J. Open Source Softw. **5,** 2338 (2020).

[50] N. Gregersen, D. P. S. McCutcheon, J. Mørk, J.-M. Gérard, and J. Claudon, A broadband tapered nanocavity for efficient nonclassical light emission, Opt. Express **24,** 20904 (2016).

[51] J. Canet-Ferrer, L. J. Martínez, I. Prieto, B. Alén, G. Muñoz-Matutano, D. Fuster, Y. González, M. L. Dotor, L.

González, P. A. Postigo, and J. P. Martínez-Pastor, Purcell effect in photonic crystal microcavities embedding InAs/InP quantum wires, Opt. Express **20,** 7901 (2012).

[52] J. M. Llorens, J. Buencuerpo, and P. A. Postigo, Absorption features of the zero frequency mode in an ultra-thin slab, Appl. Phys. Lett. **105,** 231115 (2014).

[53] J. Martín-Sánchez, G. Muñoz-Matutano, J. Herranz, J. Canet-Ferrer, B. Alén, Y. González, P. Alonso-González, D. Fuster, L. González, J. Martínez-Pastor, and F. Briones, Single photon emission from site-controlled InAs quantum dots grown on GaAs(001) patterned substrates, ACS Nano **3,** 1513 (2009).

[54] T. Pregnolato, X.-L. Chu, T. Schröder, R. Schott, A. D. Wieck, A. Ludwig, P. Lodahl, and N. Rotenberg, Deterministic positioning of nanophotonic waveguides around single self-assembled quantum dots, APL Photon. **5,** 086101 (2020).

[55] S. Rodt and S. Reitzenstein, High-performance deterministic *in situ* electron-beam lithography enabled by cathodoluminescence spectroscopy, Nano Express **2,** 014007 (2021).

[56] T. Heuser, J. Große, A. Kaganskiy, D. Brunner, and S. Reitzenstein, Fabrication of dense diameter-tuned quantum dot micropillar arrays for applications in photonic information processing, APL Photon. **3,** 116103 (2018).

[57] A. Patoux, G. Agez, C. Girard, V. Paillard, P. R. Wiecha, A. Lecestre, F. Carcenac, G. Larrieu, and A. Arbouet, Challenges in nanofabrication for efficient optical metasurfaces, Sci. Rep. **11,** 5620 (2021).

[58] J. Liu, K. Konthasinghe, M. Davanco, J. Lawall, V. Anant, V. Verma, R. Mirin, S. W. Nam, J. D. Song, B. Ma, Z. S. Chen, H. Q. Ni, Z. C. Niu, and K. Srinivasan, Single Self-Assembled InAs/GaAs Quantum Dots in Photonic Nanostructures: The Role of Nanofabrication, Phys. Rev. Appl. **9,** 064019 (2018).

[59] A. F. Koenderink, Single-photon nanoantennas, ACS Photon. **4,** 710 (2017).

[60] S. Hughes, S. Franke, C. Gustin, M. Kamandar Dezfouli, A. Knorr, and M. Richter, Theory and limits of on-demand single-photon sources using plasmonic resonators: A quantized quasinormal mode approach, ACS Photon. **6,** 2168 (2019).

[61] A. García-Etxarri, R. Gómez-Medina, L. S. Froufe-Pérez, C. López, L. Chantada, F. Scheffold, J. Aizpurua, M. Nieto-Vesperinas, and J. J. Sáenz, Strong magnetic response of submicron silicon particles in the infrared, Opt. Express **19,** 4815 (2011).

[62] J. v. d. Groep and A. Polman, Designing dielectric resonators on substrates: Combining magnetic and electric resonances, Opt. Express **21,** 26285 (2013).

[63] A. M. Raya, D. Fuster, and J. M. Llorens, Numerical study on Mie resonances in single GaAs nanomembranes, Nanomaterials **9,** 856 (2019).

[64] D. Rocco, L. Carletti, A. Locatelli, and C. D. Angelis, Controlling the directivity of all-dielectric nanoantennas excited by integrated quantum emitters, J. Opt. Soc. Am. B **34,** 1918 (2017).

[65] R. Filter, J. Qi, C. Rockstuhl, and F. Lederer, Circular optical nanoantennas: An analytical theory, Phys. Rev. B **85,** 125429 (2012).

[66] F. Minkowski, F. Wang, A. Chakrabarty, and Q.-H. Wei, Resonant cavity modes of circular plasmonic patch nanoantennas, Appl. Phys. Lett. **104,** 021111 (2014).

[67] L. Novotny and B. Hecht, *Principles of Nano-Optics* (Cambridge University Press, Cambridge, 2006).

[68] M. C. Löbl, I. Sollner, A. Javadi, T. Pregnolato, R. Schott, L. Midolo, A. V. Kuhlmann, S. Stobbe, A. D. Wieck, P. Lodahl, A. Ludwig, and R. J. Warburton, Narrow optical linewidths and spin pumping on charge-tunable close-to-surface self-assembled quantum dots in an ultrathin diode, Phys. Rev. B **96,** 165440 (2017).

[69] B. Alen, J. Martinez-Pastor, D. Granados, and J. M. Garcia, Continuum and discrete excitation spectrum of single quantum rings, Phys. Rev. B **72,** 155331 (2005).

[70] E. R. Hegblom, Ph.D. thesis, Electrical and Computer Engineering Department, University of California, Santa Barbara (1999).

[71] J. P. Lee, E. Murray, A. J. Bennett, D. J. P. Ellis, C. Dangel, I. Farrer, P. Spencer, D. A. Ritchie, and A. J. Shields, Electrically driven and electrically tunable quantum light sources, Appl. Phys. Lett. **110,** 071102 (2017).

[72] P. Munnelly, T. Heindel, A. Thoma, M. Kamp, S. Höfling, C. Schneider, and S. Reitzenstein, Electrically tunable single-photon source triggered by a monolithically integrated quantum dot microlaser, ACS Photon. **4,** 790 (2017).

[73] X. Li, S. Liu, Y. Wei, J. Ma, C. Song, Y. Yu, R. Su, W. Geng, H. Ni, H. Liu, X. Su, Z. Niu, Y.-l. Chen, and J. Liu, Bright semiconductor single-photon sources pumped by heterogeneously integrated micropillar lasers with electrical injections, Light Sci. Appl. **12,** 1 (2023).